

Learning Granular Media Avalanche Behavior for Indirectly Manipulating Obstacles on a Granular Slope

Haodi Hu, Feifei Qian[†], Daniel Seita[†]

[†]Equal advising

University of Southern California, United States

haodihu@usc.edu

Abstract: Legged robot locomotion on sand slopes is challenging due to the complex dynamics of granular media and how the lack of solid surfaces can hinder locomotion. A promising strategy, inspired by ghost crabs and other organisms in nature, is to strategically interact with rocks, debris, and other obstacles to facilitate movement. To provide legged robots with this ability, we present a novel approach that leverages avalanche dynamics to indirectly manipulate objects on a granular slope. We use a Vision Transformer (ViT) to process image representations of granular dynamics and robot excavation actions. The ViT predicts object movement, which we use to determine which leg excavation action to execute. We collect training data from 100 real physical trials and, at test time, deploy our trained model in novel settings. Experimental results suggest that our model can accurately predict object movements and achieve a success rate $\geq 80\%$ in a variety of manipulation tasks with up to four obstacles, and can also generalize to objects with different physics properties. To our knowledge, this is the first paper to leverage granular media avalanche dynamics to indirectly manipulate objects on granular slopes. Supplementary material is available at <https://sites.google.com/view/grain-cor12024/home>.

1 Introduction

Legged locomotion across granular surfaces such as sand is a formidable challenge due to factors such as insufficient support offered by the sand surface and the complex dynamics of leg-sand interactions [1, 2, 3]. It is particularly challenging for robots to climb up steep granular slopes, as the sand could easily flow underneath robot legs due to the reduced shear resistance forces [4]. Recent studies on obstacle-aided robot locomotion show the potential for legged robots to strategically leverage large obstacles within sand, such as rocks and boulders, to traverse granular and uneven terrains [5, 6, 7, 8]. However, such “obstacle-aided locomotion” strategies require specific leg-obstacle contact locations [5], thus the ability to move rocks and boulders to desired locations became essential for these strategies to apply. To address this challenge, this study aims to propose a method for a legged robot to effectively reposition obstacles on granular slopes by primarily leveraging indirect manipulation. Prior work has shown that external disturbances on a sand incline can trigger avalanche behavior [9, 10, 11], suggesting the potential for a legged robot to exploit this property to advantageously relocate obstacles on a granular surface.

In this work, we propose **Granular Robotic Avalanche Interaction (GRAIN)**, a novel learning-based method for leveraging granular avalanche dynamics for indirectly manipulating objects on a granular slope. Due to a lack of accurate simulators for simulating legged robots and avalanche behavior on granular slopes, we do all experiments in the real world. We use an RHex [12] family robot leg as an external disturbance source which performs excavation actions within a grain tank with mechanical support to form a slope. We also design a gantry structure to enable the robot leg to move to different positions for performing leg excavations. We collect training data through physical interaction and deploy our trained model in the real world with a quadrupedal robot. See Fig. 1 for our setup.

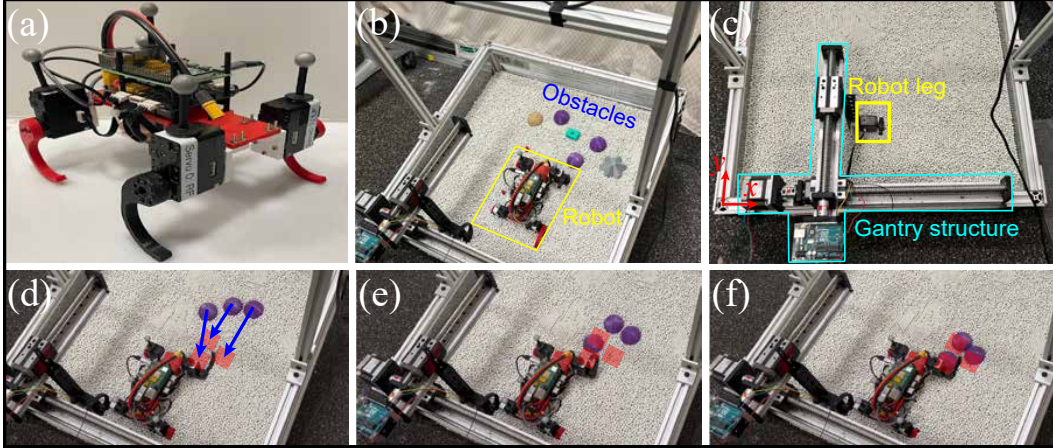


Figure 1: **Top:** (a) our quadrupedal robot and (b) a granular slope with the robot and obstacles; (c) our setup to collect data from one robot leg (highlighted in yellow) manipulating obstacles, with our designed gantry system (highlighted in cyan) for moving the leg over the granular slope. **Bottom:** (d), (e), (f) an example trial of our proposed system to manipulate obstacles on the granular slope. The three blue arrows in (d) represent the change in each obstacle’s location after applying the excavation, and the red shaded areas are targets.

Accurately predicting the granular media dynamics is essential for our proposed task, but is fundamentally challenging [1, 11, 13, 14]. To address this, we leverage learning methods in this study. We place a rigid 3D-printed obstacle on the granular slope and collect data by applying continuous robot leg excavation actions to investigate avalanche behavior. We represent the granular surface state via the current depth image and the change in depth between sequential robot leg excavations, and we also use an image to represent the leg excavation action. This enables a unified image-based input to our granular media dynamics model. We train a ViT [15] to take our proposed granular media and robot excavation action representations as input and output the object movement on the granular slope. Experiments over 30 trials suggest that our model can accurately predict object movements on a granular slope, and can generalize to objects with different physics properties.

In summary, our main contributions are as follows:

1. A novel problem formulation of using legged robots and leg excavation actions to indirectly manipulate obstacles to targets over complex, granular terrains.
2. GRAIN, a novel approach that uses image-based representations of granular dynamics and legged excavation actions to predict object movements on a granular surface.
3. Experimental results showing that a legged robot using GRAIN can move obstacles to targets, and that GRAIN outperforms an ablation and a non-learning baseline.

2 Related Work

Robot interaction with granular media: Researchers have explored robotics and granular media in locomotion and manipulation contexts. For example, researchers have enabled crawling [16, 4], hopping [17, 18], and running [19, 2, 3] over granular media by leveraging advances in granular force models [1, 13] and machine learning methods [20, 21]. We focus on the orthogonal task of leveraging the properties of granular media to manipulate objects on it. This requires some understanding of how granular media behave, which could be from direct physics analysis [22, 23, 24] or learned models [25, 26]. These models can aid common manipulation tasks involving granular media, which include pouring [27, 28, 29, 30, 31, 32], scooping and bulldozing [33], trenching [34, 14] or adjusting soil with plates [35]. In some of the most relevant prior work, Schenck et al. [36] use an image-based representation of granular media and train a convolutional neural network to predict changes in the granular media state. Similarly, we use image-based representations of granular media, but our actions are based on leg excavations instead of scooping or pouring. Moreover, we use legs of a legged robot to indirectly manipulate objects on granular media surfaces.

Locomotion over diverse terrains: Recent research has proposed methods that enable legged robots to traverse over a variety of terrains, including outdoor settings that may have sand, vegetation, rocks, or other granular media. A promising technique is reinforcement learning coupled with advanced simulators, which can help avoid significant manual engineering [37, 38]. To better handle diverse terrains, one line of work proposes *adaptation* methods, either via rapid motor adaptation [39, 40] or by encoding a family of gait methods which facilitates tuning to new terrains [41]. Other works study navigation over challenging terrains [42], which may involve climbing, jumping [43], and crawling under parkour-style settings [44, 45]. While impressive, these works study locomotion over terrains that are much sturdier than our granular surface. Furthermore, they primarily consider locomotion, whereas we focus on manipulating objects on a granular surface.

Manipulation with legged robots: While legged robots primarily use legs to move to a target location, they can also use legs for *manipulation*. For example, researchers have proposed methods for using legs to kick soccer balls [46, 47] and to push obstacles [48, 49]. A legged robot can also use two legs to stand up to better enable other legs to press against higher objects such as door buttons [50]. Other works mount an arm on top of a legged robot, and leverage methods such as optimization [51, 52] or machine learning [53, 54, 55] to allow the arm to manipulate objects. These works use legged robots for manipulation via direct contact with an object. To our knowledge, our work is the first to show a legged robot *indirectly* manipulating an object to make it reach a desired pose. To do this, the robot adjusts a granular surface that supports the object.

3 Preliminaries and Problem Statement

We consider the RHex [12] family of legged robots, with 1 DOF for each leg. We generate an *excavation action*, per leg, by commanding the leg to rotate at a constant angular speed for one circular cycle. We assume the robot lies on a granular (sand-like) surface which has a slope of Φ degrees. This surface has $K \geq 1$ rigid obstacles, and we indicate their respective positions at a given time t as $\{\mathbf{s}_t^{(1)}, \dots, \mathbf{s}_t^{(K)}\}$. The task is to move all obstacles from their initial locations to pre-specified desired locations $\{\mathbf{p}^{(1)}, \dots, \mathbf{p}^{(K)}\}$. After doing this, we may also want to move the obstacles to a second target location, and we indicate these optional (per-obstacle) target locations as $\{\mathbf{q}^{(1)}, \dots, \mathbf{q}^{(K)}\}$. Here, each $\mathbf{s}_t^{(k)} \in \mathbb{R}^2$, $\mathbf{p}^{(k)} \in \mathbb{R}^2$, and $\mathbf{q}^{(k)} \in \mathbb{R}^2$ for $k \in \{1, 2, \dots, K\}$, since we specify 2D positions over an image of the granular surface. For notational convenience, when $K = 1$ we may suppress the superscript (k) . We assume access to an overhead camera, which provides $(H \times W)$ *depth* image observations \mathbf{x}_t . The objective is to learn a policy which produces a leg excavation action \mathbf{a}_t at time t , where the robot rotates one of its legs. A *trial* consists of executing the robot’s policy until a termination criteria. We evaluate a trial’s performance by averaging the mean absolute error (MAE) distance among all obstacle positions and their respective target positions. We also use MAE to evaluate models which predict where obstacles move based on robot actions.

4 Approach: GRAIN

4.1 Image Representations of Granular Dynamics

Prior work has shown that external disturbances can trigger avalanche behavior on granular slopes [56]. Inspired by this, we aim to leverage robot leg excavation actions to cause avalanche behaviors to move obstacles to desired locations. Intuitively, the robot leg excavation location affects the avalanche area, and an obstacle’s relative position to the excavation affects how much it is influenced by the avalanche. Due to the complexities of modeling avalanche dynamics and obstacle movements on the granular surface, we learn an action-conditioned dynamics machine learning model to predict obstacle movement. Similar learned models have predicted complex physical interactions for planning robot manipulation [57, 58, 59], suggesting their utility for our task. To represent the obstacle and the granular slope surface, we use a top-view depth image, \mathbf{x}_t .

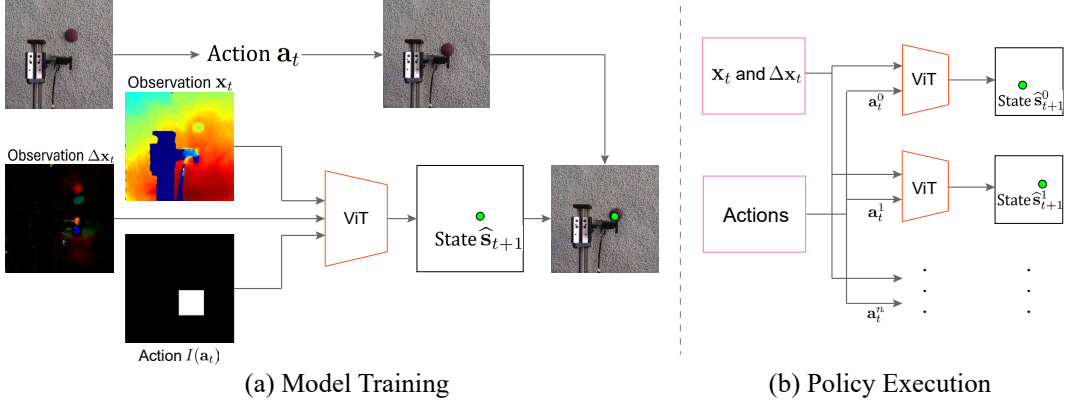


Figure 2: Overview of GRAIN. (a) The ViT has three inputs: the depth image of the granular surface \mathbf{x}_t , the change in depth before and after excavation $\Delta\mathbf{x}_t$, and the image representation of the action $I(\mathbf{a}_t)$. The output of the ViT is the prediction of the obstacle’s post-excavation location which is a 2D vector. (b) We use the trained ViT to predict object movements based on leg excavation actions. The ViT combines the current observation with candidate actions as input and predicts corresponding object movement. The ViT considers one obstacle in its output; see Sec. 4.3 for handling multiple obstacles at test time.

Furthermore, during preliminary experiments, we observed that successfully relocating obstacles often required consecutive excavations at the same location. See Fig. 3 for a visualization of grain flows with sequential excavations. To highlight this physical finding in our model, we use the change in the depth images of the granular slope surface between sequential excavation actions, denoted as $\Delta\mathbf{x}_t = \mathbf{x}_t - \mathbf{x}_{t-1}$ for $t > 0$, with $\Delta\mathbf{x}_t = 0$ (all pixels zero) if $t = 0$. We also introduce an image representation of robot leg excavation locations, which enables the action input to be spatially aligned with \mathbf{x}_t and $\Delta\mathbf{x}_t$. This may help the network better learn the avalanche behavior compared to if the action is processed separately and concatenated with downstream visual features. We discretize excavation locations to 15 locations in a 5×3 grid (see Fig. 5). We plot a white square with a side length the same as the robot leg length on a black background to represent the robot leg excavation location, $I(\mathbf{a}_t)$, where \mathbf{a}_t is the excavation location on the 2D planar surface, and I is a function that generates the RGB image representation of \mathbf{a}_t .

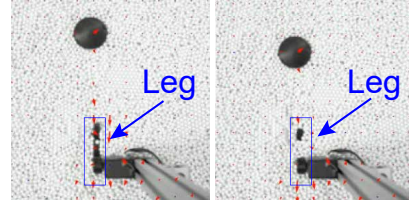


Figure 3: Granular flow for 2 sequential excavations. Red vectors represent the change of particle positions between two frames.

4.2 Training Objective for the Dynamics Model

We train a ViT to learn granular avalanche dynamics from C-shape robot leg excavations. The ViT predicts one obstacle movement on the granular slope, and we deal with multiple obstacles at test-time by repeatedly querying the model (see Sec. 4.3). The training loss \mathcal{L} is defined as:

$$\mathcal{L}(\mathbf{x}_t, \Delta\mathbf{x}_t, \mathbf{a}_t, \mathbf{s}_{t+1}) = \|F_\theta(\mathbf{x}_t, \Delta\mathbf{x}_t, I(\mathbf{a}_t)) - \mathbf{s}_{t+1}\|_2, \quad (1)$$

where F_θ is the ViT parameterized by θ that takes, as input, a channel-wise concatenation of three spatially-aligned images: the depth image \mathbf{x}_t , the change in depth $\Delta\mathbf{x}_t$, and the action representation $I(\mathbf{a}_t)$. The ViT outputs the predicted post-excavation obstacle position $\hat{\mathbf{s}}_{t+1} = F_\theta(\mathbf{x}_t, \Delta\mathbf{x}_t, I(\mathbf{a}_t))$, which we compare with the ground truth obstacle position \mathbf{s}_{t+1} on the inclined 2D surface at time $t + 1$. Since the ViT predicts continuous values, we modify the ViT’s default MLP classification header with an MLP regression header. See Fig. 2 (left) for an overview of training.

4.3 Leg Manipulation Policy

We propose a greedy strategy for manipulation, which means the robot leg performs the excavation action at the location that has a maximum obstacle movement projection on the current line

connecting the desired location and obstacle center toward the target area, described in Eq. 2:

$$\mathbf{a}_t^* = \arg \max_{\mathbf{a}_t \in \mathcal{A}} \mathbf{e}_t^T (F_\theta(\mathbf{x}_t, \Delta \mathbf{x}_t, I(\mathbf{a}_t)) - \mathbf{s}_t), \quad (2)$$

where \mathcal{A} is the set of 15 possible actions (see Fig. 5), and \mathbf{e}_t^T is a 2D unit vector that points from the obstacle center to the target location at time t (see Fig. 4, target is the shaded red square). Prior work has shown that a greedy policy for planning can be useful for object relocation tasks [60], and we hypothesize that the same may be true for our setting.

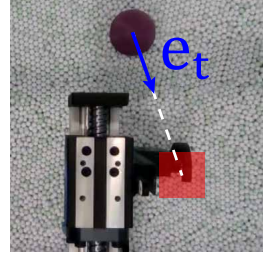


Figure 4: Example of \mathbf{e}_t .

Our model is trained using robot excavation actions with a *single* obstacle. To use the model with *multiple* obstacles, we treat multiple obstacle movement prediction as a collection of independent predictions of a single obstacle movement. In particular, we randomly select an obstacle and mask out other obstacles on the depth image input, \mathbf{x}_t , where we use a window that has a length 3 times the obstacle radius to compute the average pixel values in the windows and replace the pixel value of the obstacle with the computed averaged pixel value. Furthermore, we mask out other obstacles in $\Delta \mathbf{x}_t$, where we set the pixel values to 0 corresponding to other obstacle positions. We repeat this process for all obstacles and get the predictions of all obstacle movements. We modify our manipulation policy to fit the task; the policy now considers the sum of obstacles projected movement on lines that connect their centers to their desired locations as described in Eq. 3:

$$\mathbf{a}_t^* = \arg \max_{\mathbf{a}_t \in \mathcal{A}} \sum_{\mathbf{e}_t^T, \mathbf{s}_t} \mathbf{e}_t^T (F_\theta(\tilde{\mathbf{x}}_t, \tilde{\Delta \mathbf{x}}_t, I(\mathbf{a}_t)) - \mathbf{s}_t), \quad (3)$$

where images $\tilde{\mathbf{x}}_t$ and $\tilde{\Delta \mathbf{x}}_t$ are masked versions of \mathbf{x}_t and $\Delta \mathbf{x}_t$.

5 Experiment Setup

Existing simulators used in learning-based legged robot manipulation research, such as PyBullet [61], MuJoCo [62], or IsaacGym [63], do not support realistic robot interaction on granular media surfaces. Thus, we do all data collection, training, and experiments directly in the real world.

Experiment environment: Figure 1 illustrates our experiment setup. The main structure of the testbed is a granular trackway (60 cm $L \times$ 60 cm $W \times$ 20 cm D) filled with 6 mm plastic BBs (Matrix Tactical Systems), which have qualitatively similar rheological behavior as sand [64, 65]. The granular trackway can be tilted up to 35 degrees to emulate a wide variety of sand slopes [11] in natural environments. To study the avalanche dynamics and object movement upon different leg excavation actions, we build a gantry system with two linear actuators (one moves along the x axis and another along the y axis) to move a C-shape robot leg on a 2D surface above the granular slope. The C-shape robot leg has a diameter of 6.0 cm and a width of 2.0 cm, and the rotation center of the leg is 1.0 cm above the initial granular slope surface. The rotation frequency of the robot leg is fixed at 0.33 Hz. The robot leg uses a steel bar to attach to the table of the second linear actuator. This is sufficiently above the granular surface, so the robot avoids touching it while transitioning between consecutive excavation actions. We mount an RGBD camera (Intel RealSense 435-i) above the granular slope to record the granular flow and obstacle movement.

Data collection: We collect a dataset of 100 trials, where each trial has 10 excavation actions. The time interval between two consecutive excavation actions is 12 s to enable the robot leg to transit to different locations. Before each trial, a human operator manually smoothed the granular media to a (roughly) even granular slope with an inclination angle $\Phi = 18$ degrees. This inclination angle is close to the angle of repose [66] of the granular material used in our work, which facilitates the study of the avalanche dynamics. Once the granular surface is prepared, the human placed a 3D-printed (PLA) obstacle on the granular surface at different locations relative to the leg. For all 100 trials, a semi-spherical obstacle with a 5 cm diameter is used. The RGBD camera has a video streaming rate of 15 Hz, and it collects 640x480 RGBD images after every excavation action. The ground truth

obstacle movement is calculated based on the post-excavation RGBD image. Among the 100 trials, 36 use the same excavation location but different initial obstacle positions, 30 use the same initial obstacle position but different excavation locations, and 34 vary both the initial obstacle positions and excavation locations for each action. We use this data to train F_θ .

Evaluation: For each trial, after the human places the obstacles, a computer program randomly selects target location(s) for each obstacle. Targets can be anywhere in the robot excavation action space, as long as they do not overlap with each other. Then, the program randomly selects a method among a set of methods we test (GRAIN, a baseline, or an ablation, see Sec. 6.2) for manipulation, to reduce human bias in making initial settings easier for our method. We evaluate our dynamics model and manipulation outcomes based on the prediction error for each excavation action, using Mean Absolute Error (MAE). In test trials, we compute performance based on the final distance between the obstacle center and its desired location. The success threshold is below 2.5 cm (the radius of the obstacle) which we measure via converting pixel distances in images to centimeters. We also use the average error between prediction and ground truth as a performance evaluation.

6 Experiment Results and Discussions

6.1 Model Performance on Predicting Obstacle Movements

To evaluate the performance of our model in predicting obstacle movements, we place an obstacle on an undisturbed granular slope and test 15 excavation action locations; we reset the obstacle to the same location after each action. See Fig. 5 for a comparison between the predictions and the ground truth locations. The MAE for these 15 excavation actions is 1.13 cm, below our 2.5 cm threshold. Based on the promising MAE results, we use our trained model for planning in Sec. 6.2 and Sec. 6.3.

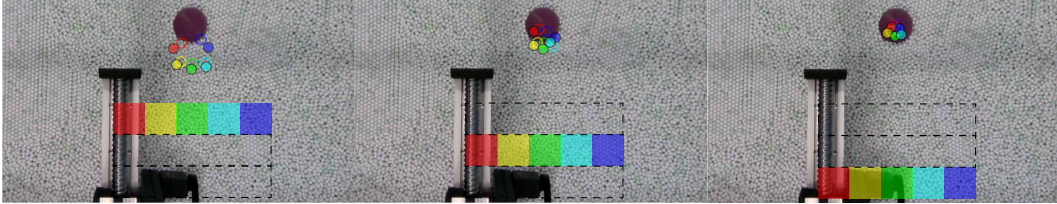


Figure 5: Obstacle movement with different excavation actions, visualized with colored squares (5 actions per image above). These $5 \times 3 = 15$ colored squares are the 15 discretized excavation actions we consider. The corresponding *solid* color circles and *empty* color circles are the trained model’s predicted obstacle positions and experiment-measured obstacle positions, respectively. (This figure is best viewed zoomed-in.)

6.2 Single Leg Manipulation Performance

We evaluate GRAIN in real-world experiments with a single leg using four types of tasks:

1. **Single obstacle with a single task:** Using $K = 1$ obstacle, with a target position \mathbf{p} .
2. **Single obstacle with sequential tasks:** Using $K = 1$ but with an additional (second) target \mathbf{q} .
3. **Multiple obstacles:** Using $K = 4$ obstacles with targets $\{\mathbf{p}^{(1)}, \mathbf{p}^{(2)}, \mathbf{p}^{(3)}, \mathbf{p}^{(4)}\}$.
4. **Unseen obstacle:** Using $K = 1$ obstacle with a target position \mathbf{p} , but where the new obstacle has a star shape and weighs twice as much as the standard obstacle we use.

We compare GRAIN against a *baseline* and an *ablation*. Our baseline is an algorithmic, non-learning manipulation strategy. The baseline randomly selects an obstacle, and the robot performs the excavation at the closest available location to the target until the obstacle has met one of two termination criteria (see next paragraph). Then, this baseline randomly selects one of the remaining obstacles to manipulate and repeats until all obstacles are selected. Our ablation investigates the importance of our image representation of the robot excavation action to the successful training of our model. We train a ViT with a lower-dimensional, 2D *vector representation* of the robot excavation action. This cannot be directly channel-wise combined with the depth-based image observations, so we instead input it to the regression header of our ViT.

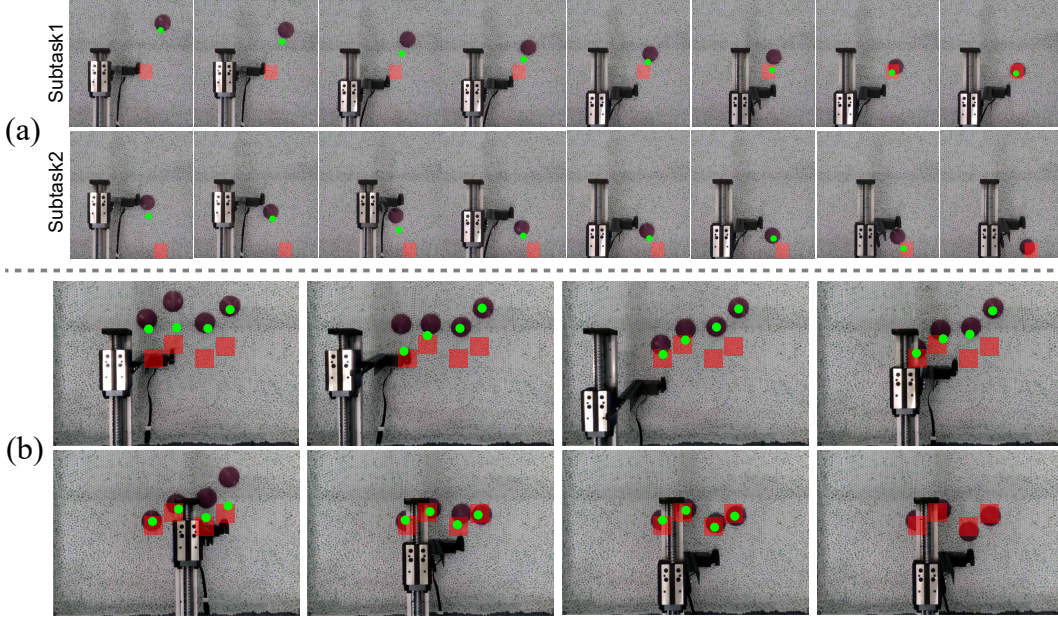


Figure 6: Single leg manipulation results, showing one trial each of (a) “Single obstacle with sequential tasks” and (b) “Multiple obstacles.” The red shaded boxes are the obstacle targets. The green dots are the predicted post-excavation locations of obstacles after the leg performs an excavation at its location.

Task	Method	MAE [†] (cm)	MAE [§] (cm)	Success rate (%)
Single obstacle with single task	Baseline	N/A	1.78(± 0.96)	80%
	Vector representation	2.34(± 0.94)	1.76(± 0.63)	80%
	GRAIN	1.66(± 0.62)	1.39(± 0.41)	100%
Single obstacle with sequential tasks	Baseline	N/A	2.24(± 1.12)	60%
	Vector representation	2.51(± 0.96)	2.17(± 0.72)	60%
	GRAIN	1.78(± 0.62)	1.42(± 0.45)	100%
Multiple obstacles ($K = 4$)	Baseline	N/A	5.12(± 3.44)	20%
	Vector representation	2.89(± 1.11)	2.21(± 0.88)	60%
	GRAIN	2.21(± 0.91)	1.85(± 0.74)	80%
Unseen obstacle	Baseline	N/A	4.34(± 2.87)	60%
	Vector representation	2.67(± 1.42)	2.49(± 1.38)	40%
	GRAIN	1.96(± 0.90)	1.91(± 0.73)	80%

[†]MAE for model predictions versus ground truth. [§]MAE for final obstacle positions versus target positions.

Table 1: We compare the quantitative performance of our method (GRAIN) versus alternative methods on four manipulation tasks. We report MAE in two columns, both using the format: Mean(± Standard Deviation), over 5 trials each. The “Baseline” method involves no prediction, hence the “N/A” in the first MAE column.

A manipulation trial terminates upon either of these conditions: (i) none of the excavation actions can take obstacles closer to their targets, or (ii) all obstacles have a small accumulated movement (≤ 0.5 cm) over 3 sequential excavations. In (i), for the baseline method, we terminate when we observe that the previous excavation action took the obstacle away from its target or reached it.

Results from Tab. 1 suggest that GRAIN outperforms the baseline and the vector representation ablation. GRAIN has a success rate $\geq 80\%$ on all manipulation tasks, while the baseline has trouble with the “Multiple Obstacles” task, and the ablation has trouble with the “Unseen obstacle” task. The baseline particularly struggles when manipulating multiple obstacles (20% success), as it does not consider other obstacle movements when manipulating one obstacle. The ablation’s granular dynamics model has a higher (i.e., worse) MAE in the predictions, which results in lower success rates versus GRAIN. We show one trial each of “Single obstacle with sequential tasks” and “Multiple obstacles” in Fig. 6. We refer the reader to the supplementary website for videos.

6.3 Quadruped Robot Manipulation Experiments

We evaluate GRAIN on the quadrupedal robot with 2 front legs as manipulators; we do not use the back legs since the robot body would likely block obstacles. Specifically, we use the same trained model as in Sec. 6.2 but we query the model at the 2 excavations where the legs are located, instead of the full set of 15. We show one trial in Fig. 7. Results in Tab. 2 suggest that GRAIN achieves higher performance (i.e., lower MAE) than the baseline or vector representation methods.

Task	Method	MAE [†] (cm)	MAE [§] (cm)	Success rate (%)
Multiple obstacles ($K = 3$)	Baseline	N/A	4.56(± 2.46)	30%
	Vector representation	3.19(± 1.34)	2.67(± 1.12)	40%
	GRAIN	2.52(± 1.08)	1.91(± 0.97)	70%

[†]MAE for model predictions versus ground truth. [§]MAE for final obstacle positions versus target positions.

Table 2: We compare the performance of GRAIN and alternative methods on the multiple obstacles task (with 3 obstacles) using the quadrupedal robot, in a similar format as Tab. 1, except statistics are over 10 trials each.

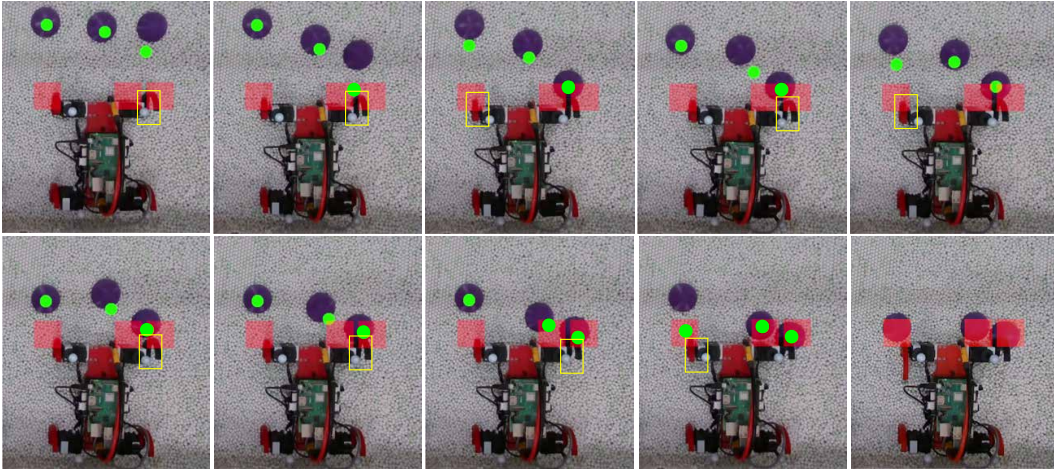


Figure 7: One trial of a quadruped robot manipulating three obstacles to reach targets (indicated with red shaded boxes). The yellow boxes highlight the leg that performs the excavation action at each step, and the green dots are the predicted post-excitation locations of obstacles after the leg performs the action.

6.4 Failure Cases and Limitations

A common failure of GRAIN with multiple obstacles occurs when the robot leg moves one obstacle to its target while simultaneously moving other obstacles too far from their targets. See Fig. 8 for an example, where two obstacles are already at their target locations (red shaded boxes), but the robot has trouble moving the third obstacle to its target (white arrow and green shaded box). The rightmost obstacle has reached its target, and further excavations will move it away from its target. Our manipulation policy only predicts obstacle movements for one step, and thus can have difficulty with tasks that require multiple-step planning, which we plan to address in future work.

7 Conclusion

In this work, we present GRAIN, a method for a legged robot to indirectly manipulate obstacles on a granular surface. We show the potential for a quadrupedal robot to advantageously leverage granular avalanche dynamics to relocate obstacles on a granular slope. We hope our work drives future research in using legged robots for manipulation and locomotion across diverse terrains.

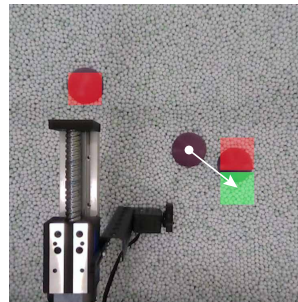


Figure 8: Failure case.

Acknowledgments

This work is supported by funding from the National Science Foundation (NSF) CAREER award #2240075, the NASA Planetary Science and Technology Through Analog Research (PSTAR) program, Award # 80NSSC22K1313, and the NASA Lunar Surface Technology Research (LuSTR) program, Award # 80NSSC24K0127. The authors would like to thank Luke Cortez for helping with preliminary data collection, and Vedant Raval for helpful writing feedback.

References

- [1] C. Li, T. Zhang, and D. I. Goldman. A terradynamics of legged locomotion on granular media. *science*, 339(6126):1408–1412, 2013.
- [2] F. Qian, T. Zhang, C. Li, P. Masarati, A. M. Hoover, P. Birkmeyer, A. Pullin, R. S. Fearing, and D. I. Goldman. Walking and running on yielding and fluidizing ground. *Robotics: Science and Systems*, page 345, 2013.
- [3] F. Qian, T. Zhang, W. Korff, P. B. Umbanhowar, R. J. Full, and D. I. Goldman. Principles of appendage design in robots and animals determining terradynamic performance on flowable ground. *Bioinspiration & biomimetics*, 10(5):056014, 2015.
- [4] H. Marvi, C. Gong, N. Gravish, H. Astley, M. Travers, R. L. Hatton, J. R. Mendelson III, H. Choset, D. L. Hu, and D. I. Goldman. Sidewinding with minimal slip: Snake and robot ascent of sandy slopes. *Science*, 346(6206):224–229, 2014.
- [5] F. Qian and D. Goldman. Anticipatory control using substrate manipulation enables trajectory control of legged locomotion on heterogeneous granular media. In *Micro-and Nanotechnology Sensors, Systems, and Applications VII*, volume 9467, page 94671U. International Society for Optics and Photonics, 2015.
- [6] F. Qian and D. E. Koditschek. An obstacle disturbance selection framework: emergent robot steady states under repeated collisions. *The International Journal of Robotics Research*, 2020.
- [7] K. Chakraborty, H. Hu, M. D. Kvalheim, and F. Qian. Planning of obstacle-aided navigation for multi-legged robots using a sampling-based method over directed graphs. *IEEE Robotics and Automation Letters*, 7(4):8861–8868, 2022.
- [8] H. Hu and F. Qian. Obstacle-aided trajectory control of a quadrupedal robot through sequential gait composition. *IEEE Transactions on Robotics*, pages 1–15, 2024.
- [9] G. Barker and A. Mehta. Two types of avalanche behaviour in model granular media. *Physica A: Statistical Mechanics and its Applications*, 283(3-4):328–336, 2000.
- [10] S. P. Pudasaini and K. Hutter. *Avalanche dynamics: dynamics of rapid flows of dense granular avalanches*. Springer Science & Business Media, 2007.
- [11] N. Gravish and D. I. Goldman. Effect of volume fraction on granular avalanche dynamics. *Physical Review E*, 90(3):032202, 2014.
- [12] U. Saranli, M. Buehler, and D. E. Koditschek. Rhex: A simple and highly mobile hexapod robot. *The International Journal of Robotics Research*, 20(7):616–631, 2001.
- [13] S. Agarwal, D. I. Goldman, and K. Kamrin. Mechanistic framework for reduced-order models in soft materials: Application to three-dimensional granular intrusion. *Proceedings of the National Academy of Sciences*, 120(4):e2214017120, 2023.
- [14] Q. Yu, C. Pavlov, W. Kim, and A. M. Johnson. Modeling wheeled locomotion in granular media using 3d-rft and sand deformation. *Journal of Terramechanics*, 115:100987, 2024.

- [15] A. Dosovitskiy, L. Beyer, A. Kolesnikov, D. Weissenborn, X. Zhai, T. Unterthiner, M. Dehghani, M. Minderer, G. Heigold, S. Gelly, et al. An image is worth 16x16 words: Transformers for image recognition at scale. In *International Conference on Learning Representations (ICLR)*, 2021.
- [16] N. Mazouchova, P. B. Umbanhowar, and D. I. Goldman. Flipper-driven terrestrial locomotion of a sea turtle-inspired robot. *Bioinspiration & biomimetics*, 8(2):026007, 2013.
- [17] J. Aguilar and D. I. Goldman. Robophysical study of jumping dynamics on granular media. *Nature Physics*, 12(3):278–283, 2016.
- [18] A. H. Chang, C. M. Hubicki, J. J. Aguilar, D. I. Goldman, A. D. Ames, and P. A. Vela. Learning to jump in granular media: Unifying optimal control synthesis with gaussian process-based regression. In *IEEE International Conference on Robotics and Automation (ICRA)*, 2017.
- [19] C. Li, P. B. Umbanhowar, H. Komsuoglu, D. E. Koditschek, and D. I. Goldman. Sensitive dependence of the motion of a legged robot on granular media. *Proceedings of the National Academy of Sciences*, 106(9):3029–3034, 2009.
- [20] J. Lee, J. Hwangbo, L. Wellhausen, V. Koltun, and M. Hutter. Learning quadrupedal locomotion over challenging terrain. *Science robotics*, 5(47):eabc5986, 2020.
- [21] S. Choi, G. Ji, J. Park, H. Kim, J. Mun, J. H. Lee, and J. Hwangbo. Learning quadrupedal locomotion on deformable terrain. *Science Robotics*, 8(74):eade2256, 2023.
- [22] H. Hinrichsen and D. E. Wolf, editors. *The Physics of Granular Media*. Wiley-VCH Verlag GmbH & Co. KGaA, 2004.
- [23] D. L. Henann and K. Kamrin. A predictive, size-dependent continuum model for dense granular flows. *Proceedings of the National Academy of Sciences*, 110(17), 2013.
- [24] K. Kamrin and G. Koval. Nonlocal constitutive relation for steady granular flow. *Physical Review Letters*, 108(17), 2012.
- [25] A. Sanchez-Gonzalez, J. Godwin, T. Pfaff, R. Ying, J. Leskovec, and P. W. Battaglia. Learning to simulate complex physics with graph networks. In *International Conference on Machine Learning (ICML)*, 2020.
- [26] N. Tuomainen, D. Blanco-Mulero, and V. Kyrki. Manipulation of granular materials by learning particle interactions. In *IEEE Robotics and Automation Letters (RA-L)*, 2022.
- [27] L. Rozo, P. Jiménez, and C. Torras. Force-based robot learning of pouring skills using parametric hidden markov models. In *9th International Workshop on Robot Motion and Control*, pages 227–232. IEEE, 2013.
- [28] M. Cakmak and A. L. Thomaz. Designing robot learners that ask good questions. In *ACM/IEEE International Conference on Human-Robot Interaction (HRI)*, 2012.
- [29] A. Yamaguchi and C. G. Atkeson. Differential dynamic programming with temporally decomposed dynamics. In *IEEE-RAS 15th International Conference on Humanoid Robots (Humanoids)*, 2015.
- [30] A. Yamaguchi and C. G. Atkeson. Differential dynamic programming for graph-structured dynamical systems: Generalization of pouring behavior with different skills. In *IEEE-RAS 16th International Conference on Humanoid Robots (Humanoids)*, 2016.
- [31] A. Yamaguchi and C. G. Atkeson. Neural networks and differential dynamic programming for reinforcement learning problems. In *IEEE International Conference on Robotics and Automation (ICRA)*, 2016.

- [32] B. Wu, F. Xu, Z. He, A. Gupta, and P. K. Allen. Squirrel: Robust and efficient learning from video demonstration of long-horizon robotic manipulation tasks. In *IEEE/RSJ International Conference on Intelligent Robots and Systems (IROS)*, 2020.
- [33] D. Millard, D. Pastor, J. Bowkett, P. Backes, and G. S. Sukhatme. Granular gym: High performance simulation for robotic tasks with granular materials. In *Robotics: Science and Systems (RSS)*, 2023.
- [34] C. Pavlov and A. M. Johnson. Soil displacement terramechanics for wheel-based trenching with a planetary rover. In *2019 International Conference on Robotics and Automation (ICRA)*, pages 4760–4766. IEEE, 2019.
- [35] M. Kobayakawa, S. Miyai, T. Tsuji, and T. Tanaka. Interaction between dry granular materials and an inclined plate (comparison between large-scale dem simulation and three-dimensional wedge model). *Journal of Terramechanics*, 90:3–10, 2020.
- [36] C. Schenck, J. Tompson, S. Levine, and D. Fox. Learning robotic manipulation of granular media. In *Conference on Robot Learning (CoRL)*, 2017.
- [37] W. Yu, D. Jain, A. Escontrela, A. Iscen, P. Xu, E. Coumans, S. Ha, J. Tan, and T. Zhang. Visual-locomotion: Learning to walk on complex terrains with vision. In *Conference on Robot Learning (CoRL)*, 2021.
- [38] J. Siekmann, K. Green, J. Warila, A. Fern, and J. Hurst. Blind bipedal stair traversal via sim-to-real reinforcement learning. In *Robotics: Science and Systems (RSS)*, 2021.
- [39] A. Kumar, Z. Fu, D. Pathak, and J. Malik. Rma: Rapid motor adaptation for legged robots. In *Robotics: Science and Systems (RSS)*, 2021.
- [40] A. Kumar, Z. Li, J. Zeng, D. Pathak, K. Sreenath, and J. Malik. Adapting rapid motor adaptation for bipedal robots. In *IEEE/RSJ International Conference on Intelligent Robots and Systems (IROS)*, 2022.
- [41] G. B. Margolis and P. Agrawal. Walk these ways: Tuning robot control for generalization with multiplicity of behavior. In *Conference on Robot Learning (CoRL)*, 2022.
- [42] A. Agarwal, A. Kumar, J. Malik, and D. Pathak. Legged locomotion in challenging terrains using egocentric vision. In *Conference on Robot Learning (CoRL)*, 2022.
- [43] G. B. Margolis, T. Chen, K. Paigwar, X. Fu, D. Kim, S. Kim, and P. Agrawal. Learning to jump from pixels. In *Conference on Robot Learning (CoRL)*, 2021.
- [44] Z. Zhuang, Z. Fu, J. Wang, C. Atkeson, S. Schwertfeger, C. Finn, and H. Zhao. Robot parkour learning. In *Conference on Robot Learning (CoRL)*, 2023.
- [45] X. Cheng, K. Shi, A. Agarwal, and D. Pathak. Extreme parkour with legged robots. In *IEEE International Conference on Robotics and Automation (ICRA)*, 2024.
- [46] Y. Ji, G. B. Margolis, and P. Agrawal. Dribblebot: Dynamic legged manipulation in the wild. In *IEEE International Conference on Robotics and Automation (ICRA)*, 2023.
- [47] Y. Ji, Z. Li, Y. Sun, X. B. Peng, S. Levine, G. Berseth, and K. Sreenath. Hierarchical reinforcement learning for precise soccer shooting skills using a quadrupedal robot. In *IEEE/RSJ International Conference on Intelligent Robots and Systems (IROS)*, 2022.
- [48] A. Rigo, Y. Chen, S. K. Gupta, and Q. Nguyen. Contact optimization for non-prehensile locomanipulation via hierarchical model predictive control. In *IEEE International Conference on Robotics and Automation (ICRA)*, 2023.

- [49] M. Sombolstan and Q. Nguyen. Hierarchical adaptive loco-manipulation control for quadruped robots. In *IEEE International Conference on Robotics and Automation (ICRA)*, 2023.
- [50] X. Cheng, A. Kumar, and D. Pathak. Legs as manipulator: Pushing quadrupedal agility beyond locomotion. In *IEEE International Conference on Robotics and Automation (ICRA)*, 2023.
- [51] H. Ferrolho, V. Ivan, W. Merkt, I. Havoutis, and S. Vijayakumar. Roloma: Robust loco-manipulation for quadruped robots with arms. In *Autonomous Robots (AURO)*, 2023.
- [52] A. Rigo, M. Hu, S. K. Gupta, and Q. Nguyen. Hierarchical optimization-based control for whole-body loco-manipulation of heavy objects. In *IEEE International Conference on Robotics and Automation (ICRA)*, 2024.
- [53] Y. Ma, F. Farshidian, T. Miki, J. Lee, and M. Hutter. Combining learning-based locomotion policy with model-based manipulation for legged mobile manipulators. In *IEEE Robotics and Automation Letters (RA-L)*, 2022.
- [54] Z. Fu, X. Cheng, and D. Pathak. Deep whole-body control: Learning a unified policy for manipulation and locomotion. In *Conference on Robot Learning (CoRL)*, 2022.
- [55] M. Liu, Z. Chen, X. Cheng, Y. Ji, R. Yang, and X. Wang. Visual whole-body control for legged loco-manipulation. *arXiv preprint arXiv:2402.16796*, 2024.
- [56] A. Daerr and S. Douady. Two types of avalanche behaviour in granular media. *Nature*, 399 (6733):241–243, 1999.
- [57] C. Finn and S. Levine. Deep visual foresight for planning robot motion. In *IEEE International Conference on Robotics and Automation (ICRA)*, 2017.
- [58] A. X. Lee, R. Zhang, F. Ebert, P. Abbeel, C. Finn, and S. Levine. Stochastic adversarial video prediction. *arXiv preprint arXiv:1804.01523*, 2018.
- [59] R. Hoque, D. Seita, A. Balakrishna, A. Ganapathi, A. Tanwani, N. Jamali, K. Yamane, S. Iba, and K. Goldberg. Visuospatial foresight for multi-step, multi-task fabric manipulation. In *Robotics: Science and Systems (RSS)*, 2020.
- [60] P. Agrawal, A. V. Nair, P. Abbeel, J. Malik, and S. Levine. Learning to poke by poking: Experiential learning of intuitive physics. In *Neural Information Processing Systems (NeurIPS)*, 2016.
- [61] E. Coumans and Y. Bai. Pybullet, a python module for physics simulation for games, robotics and machine learning. <http://pybullet.org>, 2016–2021.
- [62] E. Todorov, T. Erez, and Y. Tassa. MuJoCo: A Physics Engine for Model-Based Control. In *IEEE/RSJ International Conference on Intelligent Robots and Systems (IROS)*, 2012.
- [63] V. Makoviychuk, L. Wawrzyniak, Y. Guo, M. Lu, K. Storey, M. Macklin, D. Hoeller, N. Rudin, A. Allshire, A. Handa, and G. State. Isaac gym: High performance gpu-based physics simulation for robot learning. *arXiv preprint arXiv:2108.10470*, 2021.
- [64] R. D. Maladen, Y. Ding, C. Li, and D. I. Goldman. Undulatory swimming in sand: subsurface locomotion of the sandfish lizard. *science*, 325(5938):314–318, 2009.
- [65] J. R. Finn, M. Li, and S. V. Apte. Particle based modelling and simulation of natural sand dynamics in the wave bottom boundary layer. *Journal of Fluid Mechanics*, 796:340–385, 2016.
- [66] R. Albert, I. Albert, D. Hornbaker, P. Schiffer, and A.-L. Barabási. Maximum angle of stability in wet and dry spherical granular media. *Physical Review E*, 56(6):R6271, 1997.

A Additional Details of GRAIN

A.1 Algorithm for Image Representation of Robot Excavation Action

To highlight the relationship among the robot excavation action, avalanche behavior and obstacle movement, we introduce our image representation of the excavation actions in Sec. 4.1. The pseudocode in Alg. 1 shows how we obtain this representation. We show several examples of the image representation in Fig. 9, for different locations of the robot leg.

Algorithm 1 Image Representation of Robot Excavation Action

Require: White square size A , coordinates of robot excavation action location $\mathbf{a}_t = (x_t, y_t)$

Ensure: Output image O of size (H, W)

```

1:  $O \leftarrow$  Zero matrix of size  $(H, W)$ 
2:  $x_{\text{start}} \leftarrow \max(0, x_t - \frac{A}{2})$ 
3:  $y_{\text{start}} \leftarrow \max(0, y_t - \frac{A}{2})$ 
4:  $x_{\text{end}} \leftarrow \min(H, x_t + \frac{A}{2})$ 
5:  $y_{\text{end}} \leftarrow \min(W, y_t + \frac{A}{2})$ 
6: for  $i = x_{\text{start}}$  to  $x_{\text{end}}$  do
7:   for  $j = y_{\text{start}}$  to  $y_{\text{end}}$  do
8:      $O[i, j] \leftarrow 255$ 
9:   end for
10: end for

```

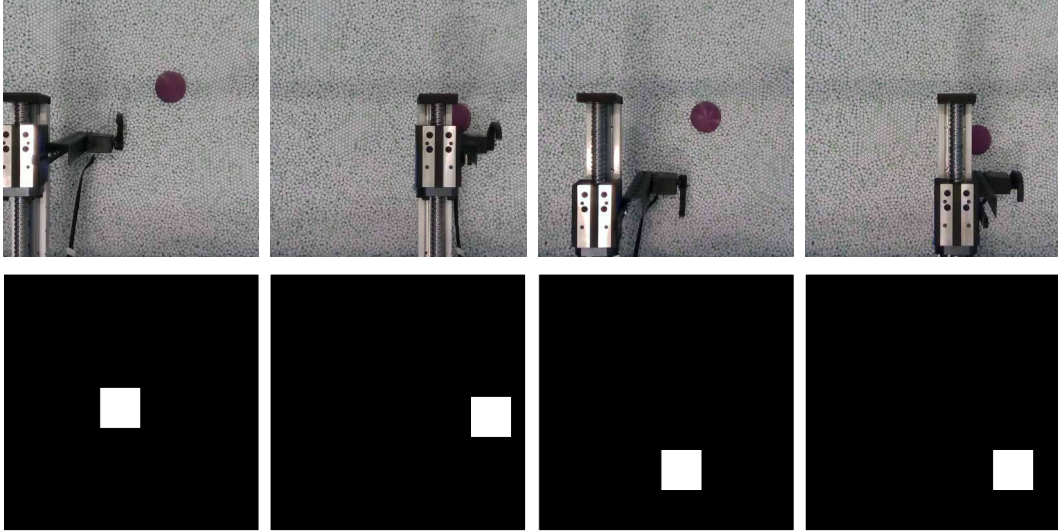


Figure 9: Additional examples of image representations of excavation actions. **Top:** RGB images of robot excavation actions. **Bottom:** The corresponding image representations of robot excavation actions.

A.2 Algorithm for Masking Obstacles in \mathbf{x}_t

Sec. 4.3 discusses how we handle multiple obstacles. In Alg. 2, we formalize our method to mask other unselected obstacles. This lets the masked images look similar to images from the single obstacle case, which we use for training the ViT. See Fig. 10 for an example of an image and its corresponding masked version (obtained via Alg. 2). During training, we use `cv2.colormap`, a package in `opencv`, to convert depth to RGB, as shown in the figure. For visual clarity, we overlay “Obstacles” and “Masked Obstacles.”

Algorithm 2 Masking Unselected Obstacles in Multiple Obstacles Manipulation

Require: Input image I of size (H, W) , window size B , list of obstacle center coordinates $\{(x_k, y_k)\}_{k=1}^{K-1}$, list of pixels sets (obstacles) $\{P_k\}_{k=1}^{K-1}$ for each coordinate

Ensure: Output image O of size (H, W)

```
1:  $O \leftarrow I$ 
2: for each  $(x, y) \in \{(x_k, y_k)\}_{k=1}^{K-1}$  with corresponding pixels set  $P$  do
3:    $x_{\text{start}} \leftarrow \max(0, x - \frac{B}{2})$ 
4:    $y_{\text{start}} \leftarrow \max(0, y - \frac{B}{2})$ 
5:    $x_{\text{end}} \leftarrow \min(H, x + \frac{B}{2})$ 
6:    $y_{\text{end}} \leftarrow \min(W, y + \frac{B}{2})$ 
7:    $S \leftarrow \{I[i, j] \mid x_{\text{start}} \leq i < x_{\text{end}}, y_{\text{start}} \leq j < y_{\text{end}}\}$ 
8:    $\text{avg} \leftarrow \frac{1}{(x_{\text{end}} - x_{\text{start}})(y_{\text{end}} - y_{\text{start}})} \sum_{(i, j) \in S} I[i, j]$ 
9:   for each  $(i, j) \in P$  do
10:    if  $x_{\text{start}} \leq i < x_{\text{end}}$  and  $y_{\text{start}} \leq j < y_{\text{end}}$  then
11:       $O[i, j] \leftarrow \text{avg}$ 
12:    end if
13:  end for
14: end for
```

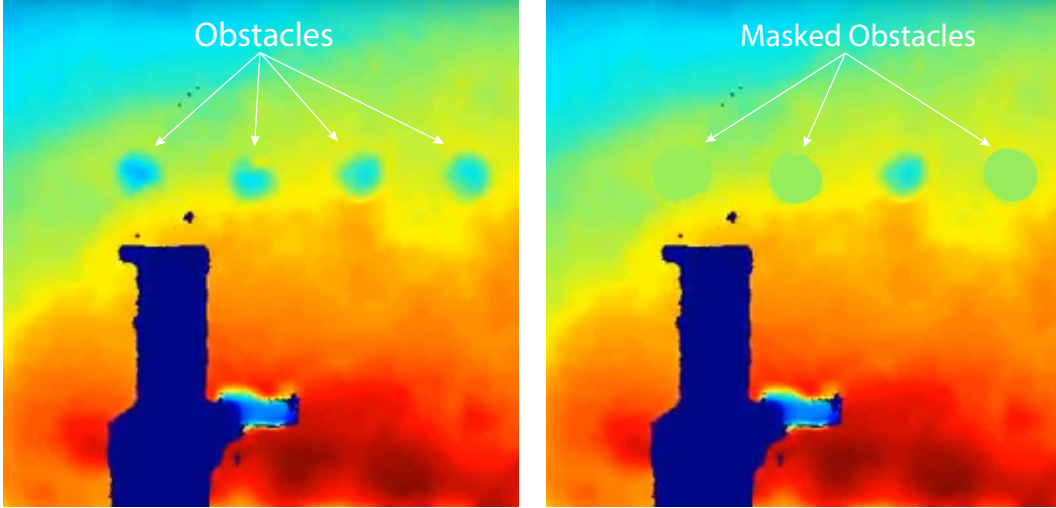


Figure 10: Example of masked image \tilde{x}_t . The left image is an example of x_t and the right image is the corresponding masked image \tilde{x}_t . Specifically, the second to the right most obstacle is the selected obstacle and other 3 obstacles are masked.

B Additional Experiment Details

B.1 Single Leg Manipulation Results

Fig. 11 shows one experiment trial for two manipulation tasks: “Single obstacle with single task,” and “Unseen obstacle.” We refer the reader to Section 6.2 for a description of what the tasks mean, and for example trials from other tasks. The statistics of all manipulation trials are shown in Tab. 1.

B.2 Multiple Unseen Obstacles Manipulation

To test our trained model’s generalization ability, we use obstacles with different shapes and weights in this task. Specifically, we use a star shape obstacle, a cuboid obstacle that has half of the weight of the obstacles used in the training dataset, and a hemisphere obstacle the same size but 4 times the weight of the obstacles used in the training dataset. All obstacles are 3D-printed. We placed these unseen obstacles on the granular slope plus the obstacle we used in the training dataset as a total of

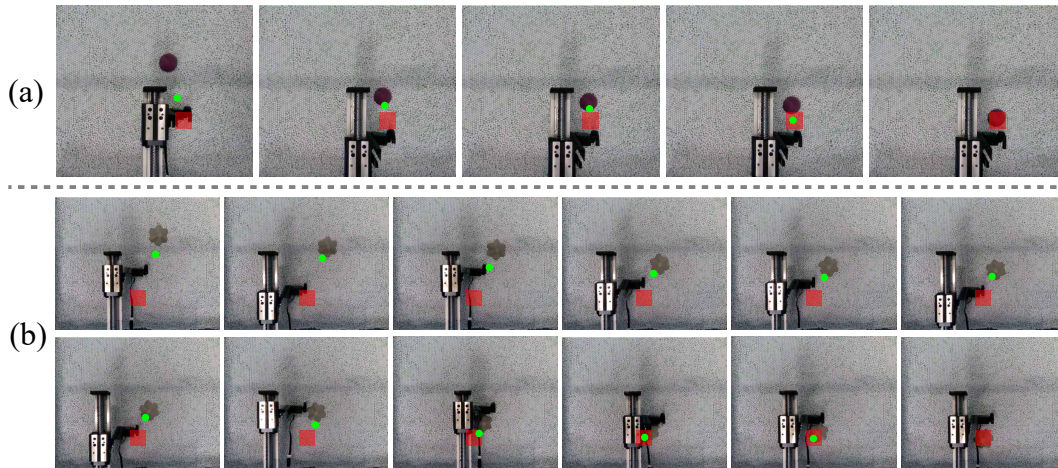


Figure 11: Single leg manipulation experiment results: (a) is “Single obstacle with single tasks,” and (b) is “Unseen obstacle.” In the above, red shaded areas are target areas. The green dots are the prediction of post-excitation locations of obstacles after the leg performs the action.

$K = 4$ obstacles with a random distribution and executed the manipulation policy. We show one manipulation trial in Fig. 12. Our system succeeds in 3 out of 5 trials.



Figure 12: Multiple Unseen Obstacles Manipulation. Red shaded areas are target areas. The green dots are the prediction of post-excitation locations of obstacles after the leg performs an action at its current location.